Journal of
Ceramic Science
and Technology

J. Ceram. Sci. Technol., **13** [2] 83-98 (2022)
DOI: 10.4416/JCST2021-00017
available online at: http://www.ceramic-science.com

Influence of Meso-Scale Material Properties on Macro-Mechanical Behavior of Three-Dimensional Four-Directional Braided Composites under Uniaxial Tensile Load

J. Xin*, Z. Fang, S. Yasong*

School of Power and Energy, Northwestern Polytechnical University, Xi'an 710072, China
received August 26, 2021; received in revised form July 5, 2022; accepted July 5, 2022

Abstract

Herein, a novel non-linear finite element model (FEM) is presented to investigate the influence of meso-scale material properties on the uniaxial tensile behavior of three-dimensional, four-directional braided composites. A reconstructed representative volume element (RVE) model is first introduced based on the micro-computed tomography (μ-CT) data and several damage modes, representing damage of yarns, matrix and the yarn/yarn and yarn/matrix interfaces, are taken into account in the meso-scale FEM model. The simulated mechanical behaviors and damage evolutions under longitudinal, transverse and off-axis tension were presented and analyzed. Furthermore, a numerical parametric study is conducted to evaluate the influence of several key meso-scale material properties on the macro stress-strain relationship and ultimate strength. The preliminary results reveal that, under longitudinal tensile load, the shear strength renders a more significant effect than the interface properties on longitudinal tensile strength because the shear stress decreases the longitudinal load capacity of yarns, however, the interface debonding only alters the complex stress state. On the other hand, under transverse tensile load, the yarn transverse direction and interface are the main load transfer routes. Thus, the transverse damage of yarns and interface damage coexist and compete, where the weaker one determines the transverse strength. The current work presents an efficient strategy to improve the performance of composites under a specific load. Also, it indicates that further work is required to obtain more accurate meso-scale material parameters.

Keywords: Four-directional braided composites, ceramic matrix composites, damage models, failure mechanism, meso-scale material properties

I. Introduction

Three-dimensional braided SiC/SiC composites are promising candidates in aviation, aerospace and marine applications due to their excellent mechanical performance, including high-temperature mechanical and thermal properties, ability to generate complex shapes, pseudo-ductile nonlinear behavior and superior delamination resistance [1]. The thermal and mechanical requirements of ceramic matrix composite (CMC) structural components can be tailored by design and optimization of fiber yarn preform at meso-scale. The effect of preform architecture at meso-scale and associated multiple failure event of constituents on material properties at structural level have been studied with experimental methods [2–5]. However, owing to the high experimental costs and periodic meso-scale structure, the concept of the representative volume element (RVE) is widely used for prediction of the composites' properties. Moreover, because of the diversity of braiding structures and multiple parameters at meso-scale, parametric studies based on numerical simulation are popularly utilized to investigate the relationship between the variation in macro-properties, adjustment of the parameters of constituent materials and the braiding process at meso-scale.

In particular, three-dimensional four-directional braided (3D-braided) preform structures consisted of four groups of inclined fiber yarns. In most RVE models of 3D braided composites, the path of yarns was assumed to be straight lines [6], while in a few studies, the path was determined as a sinusoidal curve [7]. Moreover, the shape of yarns was considered to be constant along the path, and the frequently used geometric shapes were ellipse [8], octagon [9] and hexagon [10]. But these ideal models do not contain the important features affecting the failure process of SiC/SiC composites, like the variation in yarns' sectional shapes. Therefore, the researchers have aimed to reconstruct the RVE geometric model by using scanning electron microscopy (SEM) or micro-computed tomography (μ-CT) images. In these models, the sectional shapes and trajectory of yarns caused an obvious difference with respect to the ideal meso-scale model [11–13].

Besides the meso-scale geometric model, the meso-scale material (yarn/matrix/interface) mechanical model is also important to predict macro-mechanical properties, such

* Corresponding author: jingxin@nwpu.edu.cn
co-corresponding author: yssun@nwpu.edu.cn

as strength and damage evolution. In general, anisotropic damage models are used for yarns owing to their anisotropic microstructure and multiple damage mechanisms. Moreover, the mechanical performance of CMCs with SiC matrix is not the same as the common polymer matrix composites (PMC). The SiC matrix is much stiffer (effective modulus ranging from 100 ~ 400 GPa) and more brittle than the polymer matrix, and weaker fiber/matrix interfaces were designed to change the way the matrix cracks propagate [14]. These scenarios generated significant non-linearity in stress-strain curves of SiC/SiC yarns [15]. However, mechanical simulations of meso-scale braided SiC/SiC composites are extremely rare. For instance, Zhang *et al.* utilized a simple finite element approach, where yarns were modeled as an orthotropic medium with a strain-induced damage model, to obtain the macro-scale tensile curve of woven SiC/SiC composites [16]. Ladeveze *et al.* employed an anisotropic damage model, which has been previously utilized for lamina, and calculated the pre-maximum part of the whole stress-strain curve [17]. However, the constitutive model of SiC/SiC yarn is still being investigated to better describe the anisotropic and damage evolution behavior. In the case of a resin matrix, the plastic deformation or damage models are used for different resin matrices, whereas the isotropic damage models are used due to their simplicity for brittle and porous ceramic matrices. In the case of a yarn/yarn(matrix) interface, the cohesive zone models (CZM) are extensively utilized because CZMs can describe phenomenal mechanical relationships between the tractions and interfacial separations and eliminate the stress singularity at the crack tip. Lu *et al.* [18] and Fang *et al.* [19] used CZM models to conduct parametric studies and investigate the influence of interface strength on tensile properties of 3D four-directional and 3D five-directional composites with polymer matrices. The results revealed that the interface damage was one of the key factors causing non-linearity in the stress-strain relationship. The interfaces also exist in braided SiC-based ceramic matrix composites and their influence on macro-mechanical properties should be investigated. However, some parameters are not known and cannot be directly obtained from the experiments. Also, some of these parameters are changed as a result of changes in the preparation process. Hence, it is necessary and convenient to investigate the influence of these parameters on macro-mechanical behavior. It is worth emphasizing that the parametric investigation based on numerical simulations can reduce the experimental cost and they can also result in more accurate models.

In 3D four-directional braided composites, the braiding angle exists between all inclined yarns axes and braiding directions, resulting in complex stress on yarns under off-axis load. Hence, when the composites were tested under uniaxial tension, multiple failure events, such as bridged matrix cracking and fiber break, fiber/matrix debonding along fibers, and inter-fiber matrix cracking simultaneously occurred. For example, when braided composites are under longitudinal tensile load, not only the longitudinal stress of yarns, but also the shear stress of yarns and stress-state of the yarn/yarn interface influence the strength and damage of the composites. When the braided composites are under transverse tensile load, the key mechanism controlling the transverse tensile strength changes with changing transverse strength of yarns and strength of interface. The effects of these meso-scale material parameters on macro-scale properties of braided composites can be determined by means of parametric investigation using meso-scale numerical simulations.

Herein, a new RVE model is introduced to investigate the effect of meso-scale material properties on the macro-mechanical behavior of three-dimensional four-directional braided composites under uniaxial tensile loads. With the aid of μ-CT analysis of the braiding architecture of composites, the geometric RVE model is established and converted into a discrete finite element model [20]. In the next step, the mechanical performance as well as failure processes are acquired based on the calculation of the finite element RVE model. Finally, a parametric study is conducted to assess the influence of several meso-scale material parameters, representing the effect of shear and transverse strength of yarns and interfacial strength on material properties at structural scale. As it is difficult to obtain these parameters by means of experiments, most of the preliminary values are assumed in computations based on the alternative test results and empirical estimations. Overall, the FEM analysis improves our understanding of parametric influence, and the coexistence and competition of multiple damage mechanisms under a specific load.

II. Experiment Analysis

(1) Microstructural characterization

The relevant information of these SiC/SiC composite materials has been described in detail in many other studies [3, 6, 19]. The composites were manufactured by the National University of Defense Technology (NUDT). First, the composite preform was braided from four-directional 1.2k KD-I SiC fibers yarns, each yarn making an angle of ~ 19° with the braiding direction. The total fiber volume fraction was approximately 45 %. Then, the braided SiC preform plates underwent a precursor infiltration and pyrolysis (PIP) process using a polymer precursor of liquid polyvinylcarbosilane (LPVCS) to prepare SiC/SiC composites. Finally, the dog-bone samples, of which the gage section length was 30 mm and the length and width of rectangle section were 6 mm and 3 mm, respectively, were cut from composite flat panel.

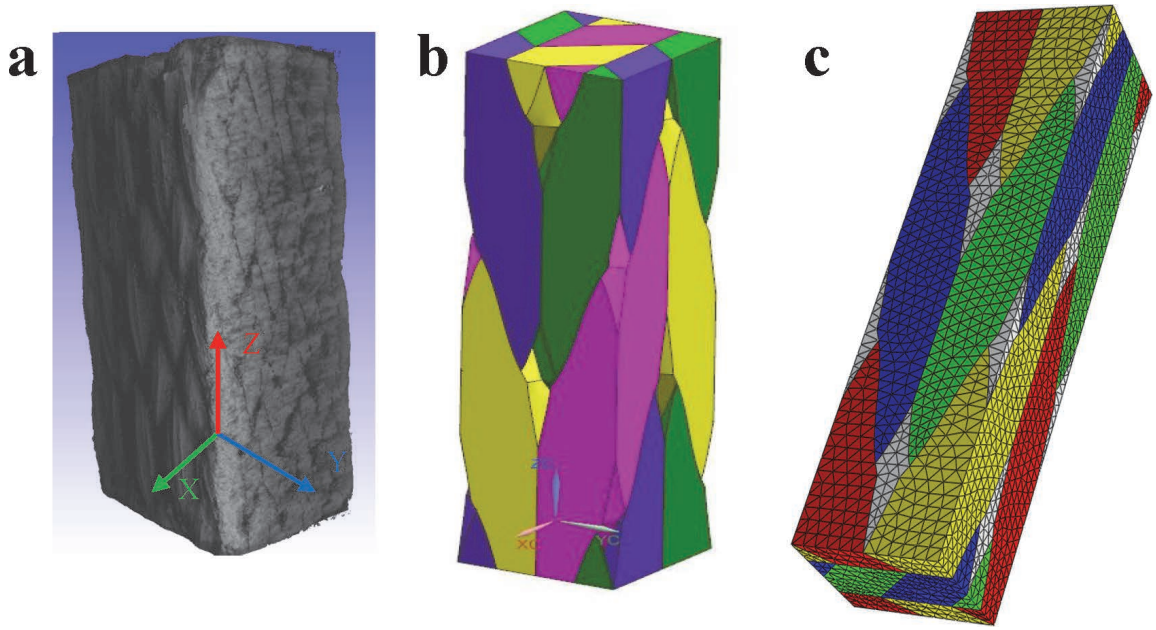

Fig. 1: (a) μ-CT model, (b) geometrical model and (c) finite element model of SiC/SiC composites at meso-scale.

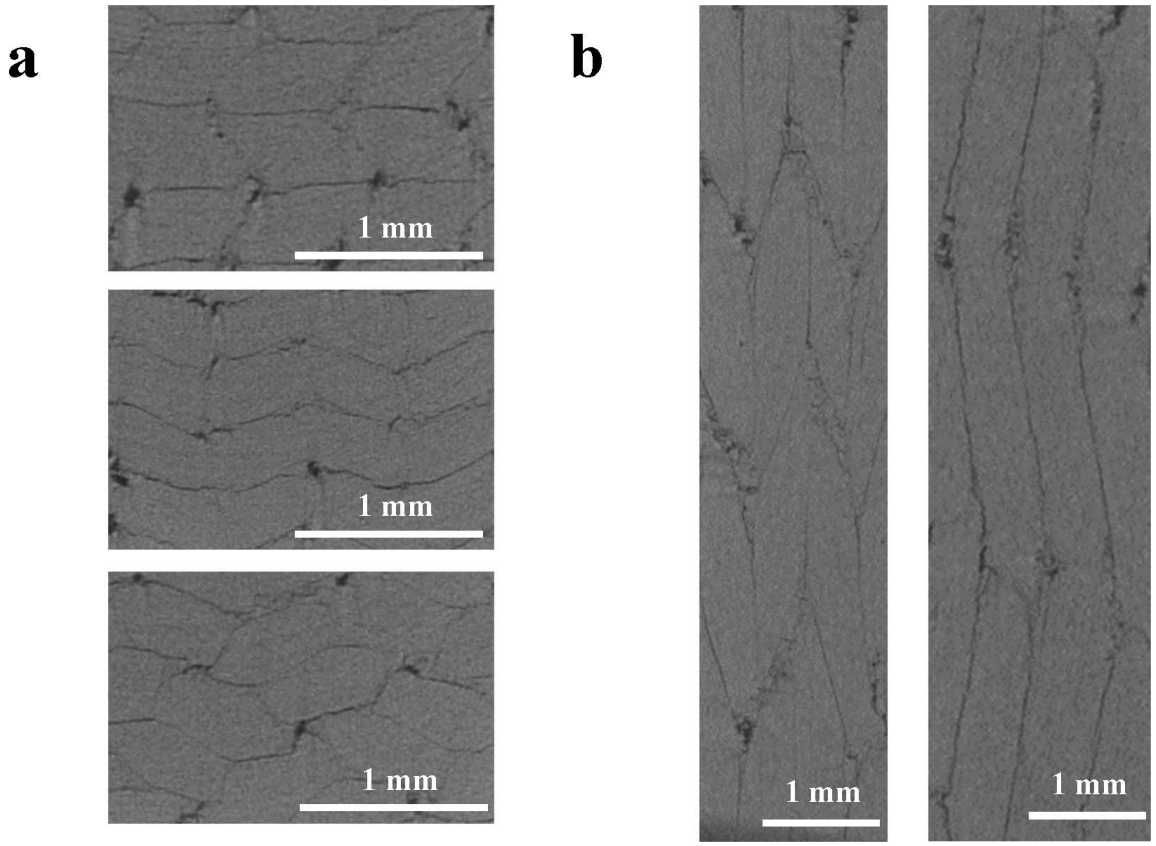

Fig. 2: Typical shapes of yarns in (a) xy- and (b) yz-plane.

The detailed microstructure of material was characterized with scanning SiC/SiC samples using μ-CT [20]. The tests were conducted in ND Inspection and Control Solution. The specimens were first scanned with a Diondo D2 X-ray microscope, and then reconstructed as 3D images in Volume Graphics (VG). Each fiber yarn and inter-yarn void could be visually distinguished with a resolution of 2.7 μm. Owing to the density difference between air (black) and SiC fiber/matrix (grey), the cracks and pores can be distinguished based on gray-scale thresholding. Fig. 1a presents the partial CT reconstruction result, the inset showing the rectangular axes x, y and z, respectively. The representative cross-section profiles in the *xz*- and *xy*-planes are presented in Fig. 2a&b, respectively. The shapes of yarns in different slices were varied along the *x-, y- and z-* directions. For instance, pentagons and parallelograms were found as the characteristic shapes in the *xy*-plane (Fig. 2a), whereas the yarns exhibited two differ-

ent types of parallelogram shapes in the *yz*-plane (Fig. 2b). However, as the fiber number in each yarn remains the same, the area of each yarn remains unchanged. In addition, at the slices where the yarn shapes were not parallelograms, discrete parts without fiber features were observed at the inter-yarn domain, which were analyzed as inter-yarn pure-matrix regions. The microscopic characterization made a distinction in the constituents of the composites, and their change regularities were visually observed.

(2) Mechanical characterization

The dog-bone SiC/SiC specimens were used to conduct the tensile experiments [3]. A Shimadzu electrohydraulic servo-controlled testing machine was used to apply the tensile load. The specimens were gripped by the edge load, passive grip interface. The alignment of the testing system was verified at the beginning of the test series. The tensile tests were conducted in a quasi-static way with a loading rate of 3 MPa/s. An Epsilon 3548 extensometer was used to record the tensile strain. The stress-strain curves are shown in Fig. 3a. The stress-strain curves were initiated with a linear response, followed by non-linear behavior. The elastic modulus and ultimate tensile strength were found to be 95 GPa and 336 MPa, respectively. Cyclic loading tests were also conducted and the results revealed the absence of any residual strain after unloading.

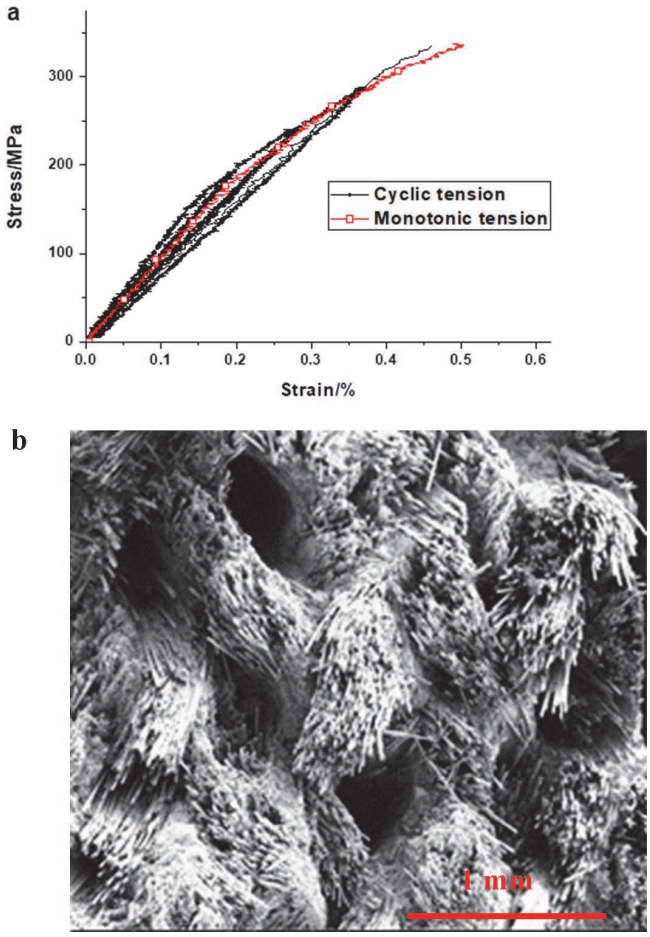

Fig. 3: (a)The stress-strain curve of 3D braided SiC/SiC composites. (b) Fracture section of 3D braided SiC/SiC composites under longitudinal tensile load.

The specimen fracture surfaces were investigated using a scanning electron microscope (SEM, ZEISS- Sigma300). The fracture surface of the tensile specimen in Fig. 3b illustrates the fiber pull-out in each yarn. In fact, multiple failure events, e.g. matrix cracking, interface debonding and fiber rupture, were all involved in the deterioration of the load capacity of the CMCs[3]. Owing to the braiding architecture, the evolution of matrix cracks was more complicated than in the unidirectional-reinforced CMCs. The cracks first initiated at the inter-yarn matrix region, and then propagated to yarn/yarn and yarn/matrix interphases. Finally, the cracks formed in yarns and exacerbated statistical breakage of the fibers, which caused ultimate failure.

III. Establishment of the RVE models

(1) Geometric models

Although the fiber preform architecture varies in real braided SiC/SiC, the braiding preforms exhibited anisotropic and periodic structures. In the next step, the sectional features of different slices in the *xy*-plane were used as input source for subsequent reconstruction of the geometric model of the RVE. Before geometric analysis, four typical planes were artificially set as planes z = 0/4 h, 1/4 h, 2/4 h, 3/4 h, where h was the height of the RVE. The detailed variation of yarns was analyzed firstly by tracking these four typical planes. At these four typical planes, all yarns showed parallelogram shapes and were tightly compacted, leaving no space for matrix intersection. As four inclined angles in the braiding process, the four groups of parallelogram-shaped yarns in these slices exhibited different deflection directions (Fig. 4a). For instance, at z = 0/4 h, the parallelograms were arranged in rows and neighboring rows exhibited opposite inclined direction. At z = 1/4 h, all the yarns showed different shapes of parallelograms, and arrays were changed to a column arrangement. At the plane with half height, the shapes of parallelograms turned back to the original plane. But the inclined angle changed compared to z = 0 h. Based on continuous analysis of CT images, it was found that parallelograms did not change their shapes, instead they moved to neighboring rows. Similarly, from z = 1/4 h to z = 3/4 h, the yarns returned to their original shape and occupied the positions in neighboring columns. When the plane went to z = h, the yarns' contour turned back to the original plane, verifying the periodicity of braiding architecture.

In each quarter, four groups of yarns moved along diagonal path, resulting in more complex deformation of shapes (Fig. 4b). From 0/4 h to 1/16 h, because of the discrepant movements of two adjacent yarns in one row, these yarns began to detach and pure SiC matrix occupied the interstice. Moreover, the acute angles of parallelograms in the neighboring row collided into the short sides and were shoved to generate a new side, turning the parallelogram into a pentagon. At 1/8 h slice, a pure matrix part lay in the middle of four pentagons, exhibiting a rhombus shape. From 1/8 h to 3/16 h to ¼ h, parallelograms from the upper and lower rows were encountered. Thus, the new sides were generated when pentagons forming turned back to points. As the variation regularity of yarns in first quar-

ter was figured out, through combined operation like rotation and replication, the entire variation of yarn preforms in RVE models was obtained.

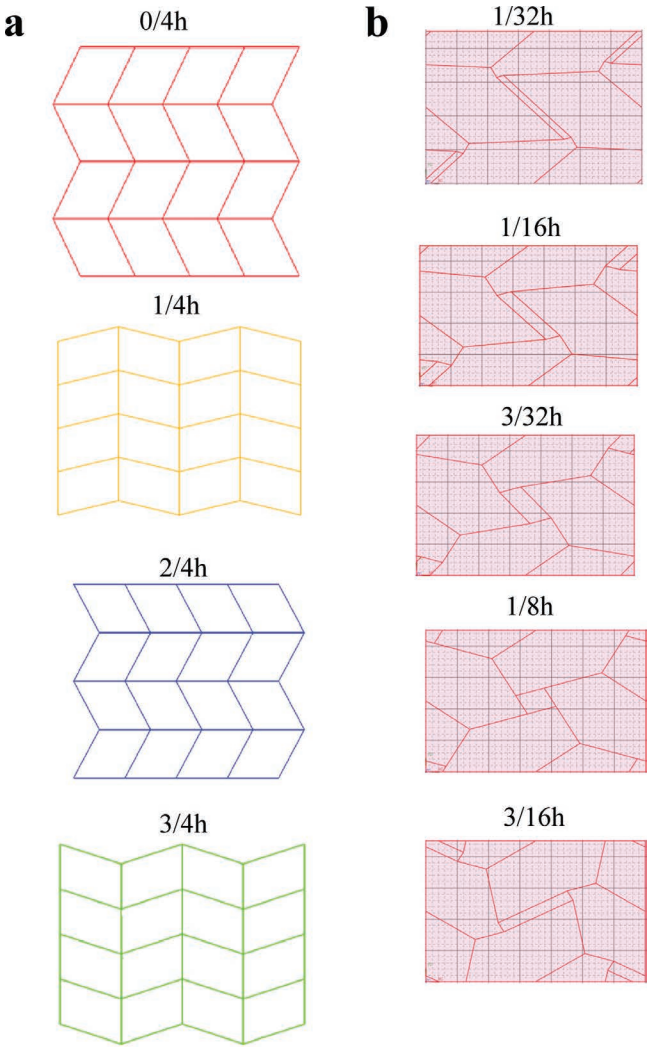

Fig. 4: (a) The shape of tows in xy-plane at z = 0, 1/4h, 1/2h and 3/4h. (b)The shape of tows in *xy*-plane at *z* = 1/32*h*, 1/16*h*, 3/32*h*,1/8*h* and 3/16*h*.

The RVE reconstruction model was established after analysis of the typical geometry and motion of yarns. The yarns' sections in the 0 h, 1/8 h and 1/4 h slices were extracted from a large number of μ-CT sliced 2D images and averaged geometric measurements were calculated for reconstruction modeling. Although the section shape altered along the trajectory, the trail of each yarn's centroid was a straight line. The reconstructed model (Fig. 1b) described the real architecture of the braiding preform, in which a bit of pure matrix existed between the snugly compacted yarns. The dimensions in x-, y- and z-direction were 1.4 mm, 0.9 mm and 4.6 mm, respectively.

(2) FE discretization

The finite element model of the RVE was built based on the previously developed geometric model. All the matrix and yarns were discretized into a second-order tetrahedral element. The meshes in bottom, left and front faces were copied to top, right and back faces, to keep periodic displacement during finite element simulation using the multi-point constraint method.

Moreover, the zero-thickness, six-node cohesive elements (COH3D6) were utilized to represent the debonding behavior at yarn/yarn or yarn/matrix interface. The regular cohesive element generating method, i.e., *offset mesh tool*, in ABAQUS could not be directly used because double layers were produced at yarn/yarn interphase. Thus, a scripted code was used to guarantee that one pair of yarn/yarn interphases contains only one group of cohesive elements [20]. The mesh of the entire finite element model of the RVE is shown in Fig. 1c.

IV. Progressive damage model

(1) Damage model for yarns

The elastic behavior of yarns was usually considered as transverse isotropic. The direction along the fibers was defined as the longitudinal directional (1) of the yarn, and the cross-section perpendicular to fiber direction was defined as the transverse plane (2, 3) in which mechanical properties were considered to be isotropic. The homogenized stiffness matrix of mesoscopic yarns had five independent constants, which were calculated based on a hierarchical method proposed by Kuhn [21]. As the load increased, the damage emerged and the linearity of stress-strain behavior was violated. To predict the initiation of damage, the three-dimensional Hashin failure criteria [22] were utilized. As the current research is focused on tensile behavior, only two tensile failure modes were considered. The damage criteria for the longitudinal and transverse directions are:

$$F_L=\left[\left(\frac{\sigma_1}{S_1}\right)^2+\alpha\left(\frac{\sigma_{12}}{S_{12}}\right)^2+\alpha\left(\frac{\sigma_{13}}{S_{13}}\right)^2\right]^{1/2} \quad (1)$$

$$F_T=\left[\left(\frac{\sigma_2+\sigma_3}{S_2}\right)^2+\left(\frac{\sigma_{23}^2-\sigma_2\sigma_3}{S_{23}}\right)+\left(\frac{\sigma_{12}}{S_{12}}\right)^2+\left(\frac{\sigma_{13}}{S_{13}}\right)^2\right]^{1/2} \quad (2)$$

where S_1, S_2, S_{12}, (S_{13}) and S_{23} are the tensile strength in direction 1 and 2, shear strength in 12 (13) and 23 planes, respectively. And alpha refers to a coefficient considering the contribution of the shear stresses to the tensile damage initiation criterion. The damage initiation was triggered once one of these criteria functions equals to or is greater than 1.

After the damage initiation, the damage evolved progressively and caused degradation of the material stiffness. Here, a strain-based continuum damage model was used to describe the multiple progressive damage process of the yarns. The transverse tensile behavior of the yarns was initially linearly elastic until maximum stress, then the stress decreased as the strain increased. A damage parameter d_T was defined as damage parameter in the transverse direction, of which the evolution was also based on the fracture energy:

$$d_T=1-\frac{1}{F_T}\exp\left[(1-F_T)L_cS_T^2/E_TG_m\right] \quad (3)$$

where L_c is the characteristic length of the C3D10 tetrahedron elements, and G_m is the fracture energy of the matrix.

As mentioned previously, due to the weak fiber/matrix interface and comparable elastic modulus between SiC fibers and brittle SiC matrix, the damage initiation was triggered far below the maximum stress. The non-linear stress-strain behavior of the unidirectional-reinforced SiC/SiC composites was attained using the micromechanical model of CMCs [14, 15, 23], and was utilized to build the longitudinal damage model of the yarn. Another damage parameter (d_L) with four subsection functions was introduced to calculate the damage state during elastic, matrix cracking, fiber breaking and yarn rupture stages. During the last stage, the stress-strain behavior was split into ascending and descending sections, where the pre-peak region adopted a damage evolution similar to stage two. In the post-peak region, the localized yarn ruptures were observed, so a general expression similar to d_T was utilized:

$$d_L = \begin{cases} 0 \\ d_1\left(1-exp\left(-\left(\dfrac{F_L-1}{m_1}\right)^{n_1}\right)\right) \\ d_2\left(1-exp\left(-\left(\dfrac{F_L-1}{m_2}\right)^{n_2}\right)\right)+d_{1\_max} \\ d_3\left(1-exp\left[\dfrac{(1-F_L)L_c S_L^2}{E_L G_f}\right]/F_L\right)+d_{2\_max} \end{cases} \tag{4}$$

where G_f is the fracture energy in the longitudinal direction, and d_i, m_i and n_i are the parameters in damage model.

The effective stiffness matrix for the damaged yarns is computed as follows:

$$C(d) = \begin{bmatrix} (1-d_f)C_{11} & (1-d_f)(1-d_m)C_{12} & (1-d_f)(1-d_m)C_{13} & & & \\ (1-d_f)(1-d_m)C_{12} & (1-d_m)C_{22} & (1-d_m)C_{23} & & 0 & \\ (1-d_f)(1-d_m)C_{13} & (1-d_m)C_{23} & (1-d_m)C_{33} & & & \\ & & & (1-d_f)(1-d_m)C_{12} & 0 & 0 \\ & 0 & & 0 & (1-d_f)(1-d_m)C_{12} & 0 \\ & & & 0 & 0 & (1-d_m)C_{12} \end{bmatrix} \tag{5}$$

where C_{ij} are the stiffness coefficients of undamaged stiffness matrix.

(2) Damage model of pure matrix

The stress-strain behavior of SiC matrix was linear-elastic before failure and quickly lost load capacity after maximum stress. Nevertheless, because the volume fraction of matrix was quite low in the RVE model, the matrix damage displayed a negligible influence on the degradation behavior of the composites' load capacity. For simplicity, the damage model utilized the maximum stress criterion for damage initiation, and the single-state variable d_m was utilized for the stiffness reduction behavior of the post-peak failure process. The formula of the damage evolution of the SiC matrix was the same as the equation for the yarn's transverse damage.

The constitutive models of the yarn and matrix were implemented by means of the user-defined subroutine UMAT [20], in which the stress and tangent stiffness at integrated points were updated. The stress was easily obtained when the effective stiffness matrix C_d was calculated, and the tangent stiffness was given as

$$\frac{\partial \Delta\sigma}{\partial \Delta\varepsilon} = C_d + \left[\left(\frac{\partial C_d}{\partial d_m^v} : \varepsilon\right)\left(\frac{\partial d_m}{\partial F_m} : \frac{\partial F_m}{\partial \varepsilon}\right) + \left(\frac{\partial C_d}{\partial d_f^v} : \varepsilon\right)\left(\frac{\partial d_f}{\partial F_f} : \frac{\partial F_f}{\partial \varepsilon}\right)\right]\frac{\Delta t}{\Delta t + \eta} \tag{6}$$

where Δt is the time increment, and η is the viscosity parameter which improves the convergence by controlling the rate at which the regularized damage variables d_{ISV}^v approach the true damage variables d_{ISV} using a viscous model:

$$\dot{d}_{ISV}^v = \frac{1}{\eta}\left(d_{ISV} - d_{ISV}^v\right)(ISV = f, m) \tag{7}$$

Table 1: Parameters of tows' constitutive model.

E_1/GPa	E_2/GPa	G_{12}/GPa	G_{23}/GPa	μ_{12}	μ_{23}
99	76	31	29	0.24	0.28

S_{L1}/MPa	d_1	n_1	m_1	S_{L2}/MPa	d_2	n_2	m_2
100	0.28	1.8	3.0	600	0.75	4	12.5

S_{L3}/MPa	d_3	G_f/N·m^{-1}	S_2/MPa	S_{12}/MPa	S_{13}/MPa	S_{23}/MPa	η
3500	0.24	0.5	160	160	160	160	0.001

* Parameters μ_{12} and μ_{23} are the Poisson's ratios of tows in xy(xz)-plane and yz-plane, respectively.

(3) Damage model of yarn/yarn and yarn/matrix interfaces

The interface in the meso-scale RVE model referred to the yarn/yarn and yarn/matrix interfaces. The detailed theory and numerical application of the CZM model can be found in the ABAQUS manual document [23]. The constitutive equation is built in terms of three components of tractions and separations between two surfaces with initial zero thickness. In the elastic stage, the initial stiffness K should be carefully set to guarantee the displacement continuity at the interface and prevent the interpenetration of the crack faces. In the linear softening stage, the quadratic nominal stress criterion (QUADS) was employed as the damage initiation criterion and the damage evolution was defined based on fracture energy.

Owing to the braided preform complexity, it is not easy to experimentally measure the material parameters of the yarn/yarn interface. As an alternative and preliminary overture, the interface property was characterized by conducting a three-point bending experiment on a short-beam SiC/SiC specimen. The mid-plane inter-yarn failure and corresponding stress drop were clearly observed in the test. As the standard ASTM-D2344 [24] points out, the as-determined short-beam strength reflects the shear property. Thus, the calculated shear strength was adopted as the shear strength of the inter-yarn interphase. For this study, to simplify the analysis, the interface strength in three directions was assumed to be the same. And interphase fracture toughness G_i equals G_m, as it was observed to be a thin and porous matrix in micro-scale tests.

The parameters used in UMAT are given in Table 1 ~ 3. In the previous study, several tests were conducted to obtain the modulus and strength of SiC fibers, matrix crack evolution and fiber/matrix debonding behavior. All these properties were adopted in the building of the meso-scale constitutive models. The rest of parameters, such as transverse tensile and shear properties, were set on the basis of previous investigation and adjusted according to calculated results. Subsequently, a parametric study was conducted to evaluate the influence of those key meso-scale material properties on the macro stress-strain relationship and ultimate strength.

Table 2: Parameters of matrix's constitutive model.

E/GPa	μ	S/MPa	G_m/N·m^{-1}	η
61	0.287	120	0.1	0.001

Table 3: Parameters of interface cohesive zone model.

E/GPa	S/MPa	G_i/N·m^{-1}
1000	80	0.1

V. Results and Discussion

Firstly, the finite element model of RVE was subjected to tensile loads along the z- and y-direction, and shear load on the yz-plane, respectively. The *equation* tool was used to keep periodic displacement consistency in each pair of opposite faces, which guaranteed that the calculated results represent the macro-scale behavior of braided composites. Then several off-axis load tests were simulated on the yz-plane with different off-axis loading angles. The calculated results were compared with the Tsai-Hill failure model. Finally, the parametric investigation was conducted in longitudinal and transverse direction with changes in different parameters.

(1) Tensile simulation results in yz-plane

The calculated stress-strain curve of tension in the z- and y-direction, and shear in the yz-plane are shown in Fig. 5. The modulus and strength in the longitudinal direction are higher than those in the transverse direction, which is the result of different damage interaction and evolution at meso-scale.

(a) *Damage evolution in longitudinal tension*

The mechanical behavior and damage evolution in longitudinal tension were analysed in detail in previous work [20]. As shown in Fig. 6a, the longitudinal damage of the yarns and matrix damage were initiated earlier when the macro strains were about 0.13 % and 0.17 %, and the transverse damage of the yarns and interface became apparent near failure. The macroscopic damage under longitudinal tensile load was controlled by the longitudinal damage of the yarns. In addition, the macro fracture strain was lower than the fracture strain of the yarns calculated with

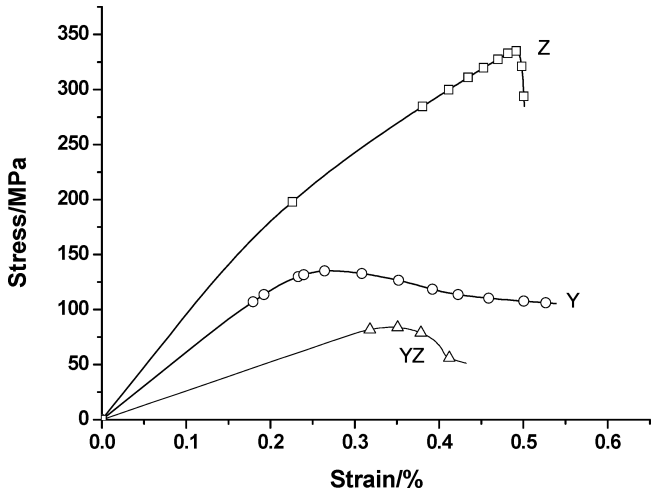

Fig. 5: Calculated stress-strain curve of tension in z- and y-direction, shear in yz-plane.

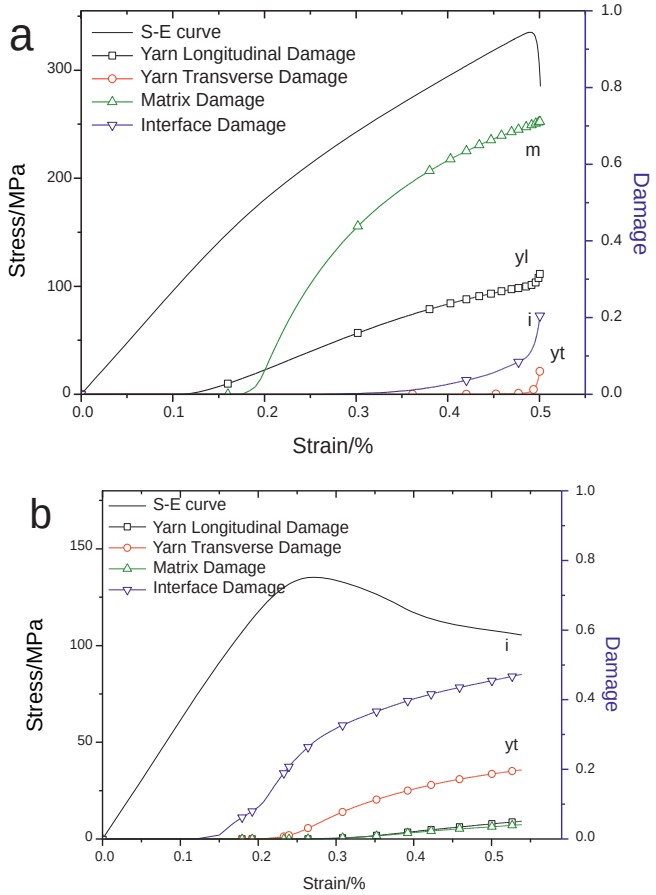

Fig. 6: The stress-strain curve of RVE and meso-scale multi-modes damage evolution under (a) longitudinal and (b) transverse tensile load.

Curtin's unidirectional CMCs model [23], indicating that multiple and localized failure events result in rupture before expected.

The stress concentration caused by the braiding architecture in the RVE model under longitudinal tensile stress of 1 MPa is shown in Fig. 7a. In the central region of the matrix, matrix damage started and then grew along the z-direction, compassing the yarn/matrix interface and penetrating into the yarns. At a macro strain of 0.14 %, the intra-yarn transversal crack distribution in the RVE is shown in Fig. 7b, where four damaged planes are observed, which are correlated to four typical matrix-rich planes. Finally, fibers began to rupture statistically owing to their dispersion. The distributions of longitudinal damage when the macro strains were 0.35 % and 0.50 % are presented in Figs. 7c and d. The damage grew more quickly at damage initiation places, leading to total failure of the composites. Nevertheless, at that time, the vast majority of elements away from failure points presented low damage states. These results confirmed that, although the SiC/SiC composites had undergone global degradation process, the meso-scale braiding structure intensified the local stress concentration and multiple damage, leading to ultimate rupture of the CMCs.

(b) ***Mechanical behavior and failure process in transverse tension***

The stress-strain curve of composites in the transverse tension is significantly different from the stress-strain curve in the longitudinal tension. The curve remained almost linear before the maximum stress and exhibited prominent ductility with a gradual decrease in load capacity. Fig. 8 shows the Von Mises stress, σ_{22} and σ_{12}, of the yarns and S_n of the interface when the transverse tensile stress is 1 MPa, which indicated that stress concentration is not severe. The normal transverse stress (σ_{22}) and shear stress (σ_{12}) are the main stresses on yarns, where the inclination angle of the yarns induces the latter. The stress concentration mainly occurred at the yarn/yarn interface, in general, and the interface connecting differently orientated yarns, in particular. Fig. 6b also presents how the interface damage and transverse damage of the yarns were the main damage mechanisms under transverse tension.

Fig. 9 presents the distribution of interface damage and transverse damage of the yarn when the strains are 0.16 %, 0.23 %, 0.28 % and 0.45 %. At the macro strain of 0.16%, damage was initiated at the stress concentration region of the inclined interface and gradually propagated. At the macro strain of 0.23 %, the interface damage propagated around the inclined interface and exacerbated at the initiation region, leading to the obvious yarn/yarn separation. At the macro strain of 0.28 %, the transverse tensile load reached the maximum value. At this stage, part of the interface started to fail and lost load transfer ability. The sharp drop in load is not observed at the maximum stress because the main load-bearing element (yarns) remained intact. However, the yarns started to get damaged after the initiation of maximum stress near the interface region. The transverse tensile damage was extensive and related to the macro transverse tensile load. At the same time, the load transfer was not continuous and the constraints between yarns were lost due to the interface failure. In the local region, bending and extrusion of yarns led to a complex stress state at the intersecting regions between yarns. The longitudinal damage of the yarns started and resulted in the ultimate failure of the 3D braided composites. Overall, despite the low transverse strength, the composites exhibited load-bearing capacity after the maximum stress and did not lead to abrupt failure due to the braided structure.

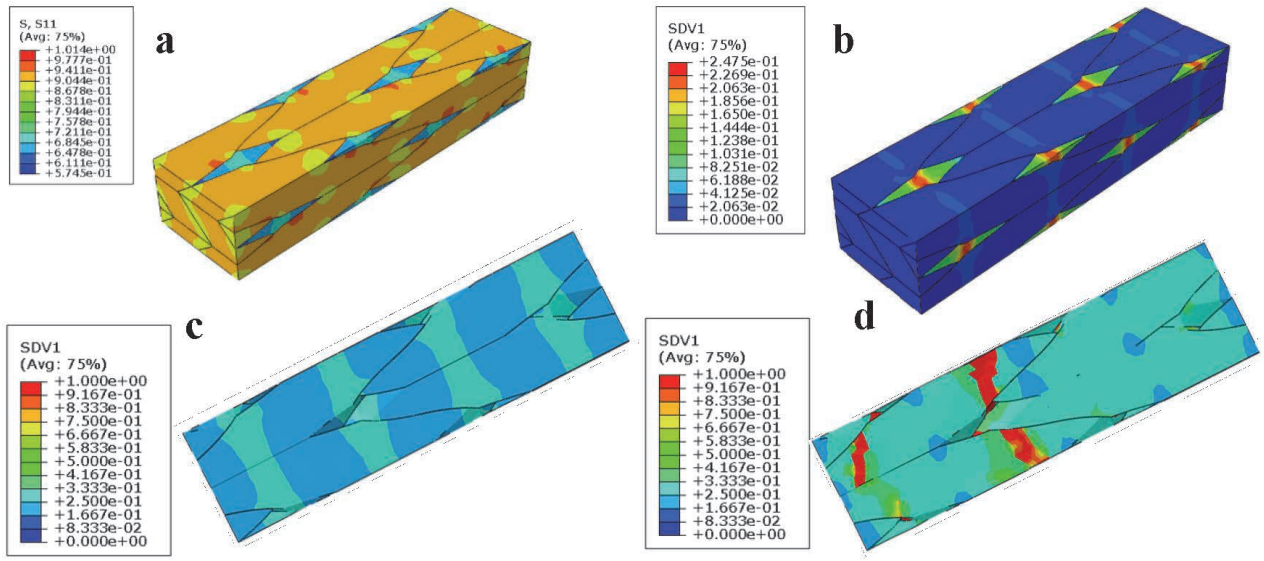

Fig. 7: (a) The stress contour in the 1-direction of tow and matrix element at macro longitudinal stress of 1 MPa. (b)The damage state variable of tows in longitudinal direction and matrix at a macro strain of 0.14%. The damage state variable of tows in longitudinal direction and matrix at a macro strain of (c)0.36%, and (d)0.50%.

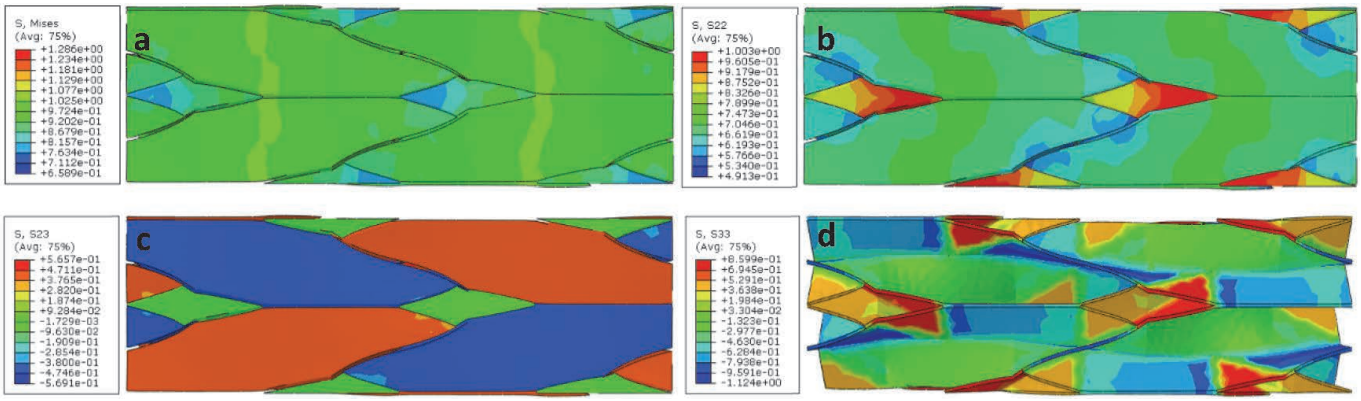

Fig. 8: (a) Mises stress and the stress contour in the (b) 22-direction and (c) 12-direction of tow and (d) tensile stress of interface element at macro transverse stress of 1 MPa.

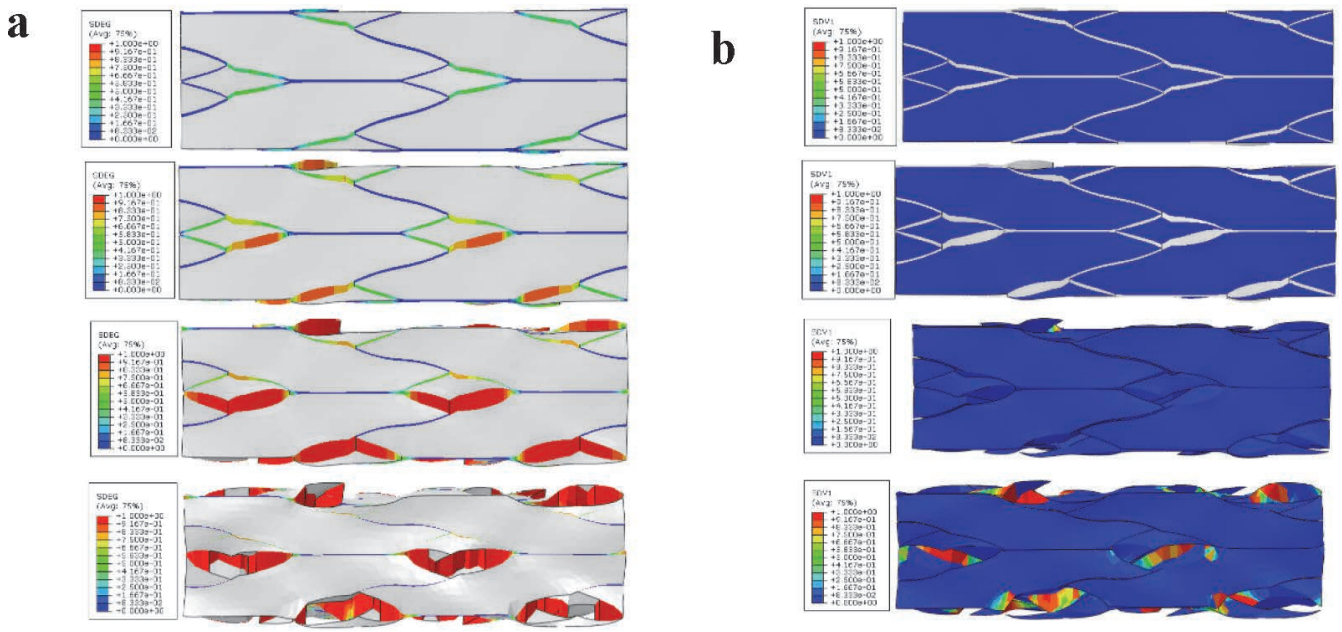

Fig. 9: The contour of (a) interface damage and (b) transverse damage of tow under transverse tensile load at a macro strain of 0.16 %, 0.23 % 0.28 % and 0.45 %.

(c) ***Stress-strain behavior and strength simulation in off-axis tension***

The different mechanical performance in longitudinal and transverse direction shows the anisotropic modulus, strength and damage evolution of braided SiC/SiC. In the next step, the off-axis tensile properties were simulated using the RVE model with different combinations of normal and shear stress in yz- and xy-plane. Besides the longitudinal (0°) and transverse (90°) tension, tensile load simulations were also conducted with off-axis angles of 15°, 30°, 45°, 60°, 75°, respectively. The off-axis angle θ refers to the angle between tensile load direction and z-direction of the composites.

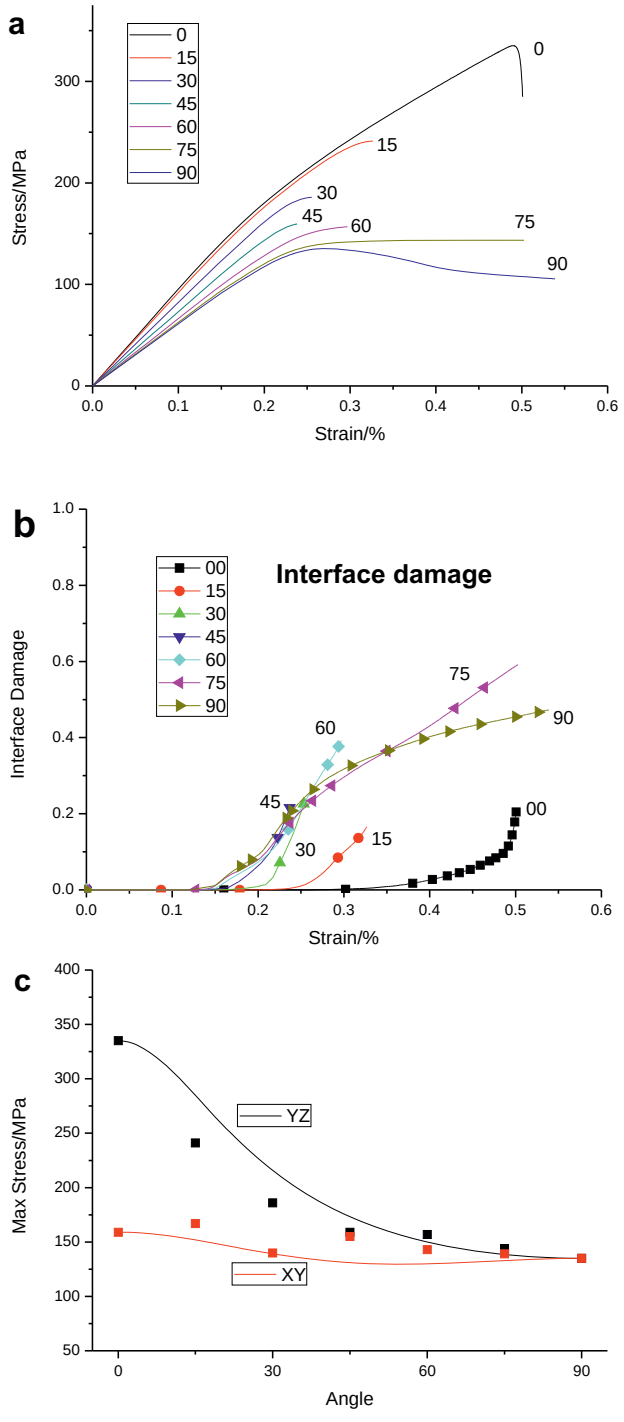

Fig. 10: (a) Stress-strain curve, (b) interface damage evolution (c) strength of SiC/SiC under off-axis tensile load.

The calculated stress-strains with different off-axis angles are shown in Fig. 10a. All the off-axis curves were located between the curve of 0° and 90°. As the off-axis angle increased, the modulus and strength decreased. However, the load-capacity decreased more mildly, from an abrupt drop at small off-axis angle to progressive decay at a large off-axis angle. The damage evolution analysis revealed that as angles increased, yarn longitudinal damage decreased and yarn transverse damage increased. The interface damage evolutions with different angles are show in Fig. 10b, which indicated that when the angle was greater than 15°, the initiation and evolution of interface damage were similar. In addition, the interface damage state at maximum stress varied between 0.18 – 0.27 with different off-axis angles, exhibiting more stable evolution regularity than other damage mechanisms.

The off-axis tensile strengths, defined by the maximus stresses in the stress-strain curve, are presented in Fig. 10c. The strength in the yz-plane decreased fast at small angles, and decayed more gently as the off-axis angle grew. The strength variation in the xy-plane was not obvious, owing to the similar structure in the x- and y-direction. In addition, the Tsai-Hill strength criterion was plotted, and the parameters in the model, tensile and shear strength, were simulated. The correlation in the yz-plane was good when the off-axis angle was greater than 45°. At small angles, the Tsai-Hill strengths were a little more than the simulated ones, and the maximum difference was within 15 %. Once the basic tensile and shear strength were obtained, the Tsai-Hill strength criterion could be used for rough estimation of multi-axis strength prediction.

(2) Parametric investigation

The simulation results above showed that multiple failure mechanisms interact at meso-scale and generate anisotropic mechanical behavior of braided SiC/SiC. The shear effect of yarns and interface damage evolution would affect longitudinal tensile behavior. And the transverse tensile effect of yarns and interface damage evolution would affect transverse tensile behavior. So these parameters would also affect off-axis loads. As mentioned in Section IV, the material parameter for the yarns' shear strength effect was assumed in advance according to previous reports, and the short-beam bending test was used to estimate the interface strength. In the following sections, the influences of these parameters are systematically analyzed.

(a) ***Influence of shear stress of yarns on longitudinal tension***

In yarn longitudinal damage criterion (Eq. 1), shear stresses (S_{12} and S_{13}) influence the longitudinal failure process. Rajan *et al.* [25] have built a micromechanical model to elaborate that the shear stress causes stress concentration at the cross-section of the fibres and decreases the yarn strength under off-axis tensile load. Herein, the quantitative impact of shear stresses on the tensile strength of yarns is not experimentally investigated. Although there were two parameters (α and S_{12}/S_{13}) in the shear stress term in Eq. 1, only one of them is considered an independent

parameter. So, α was set at 1, and S_{12} and S_{13} were changed for the parametric research.

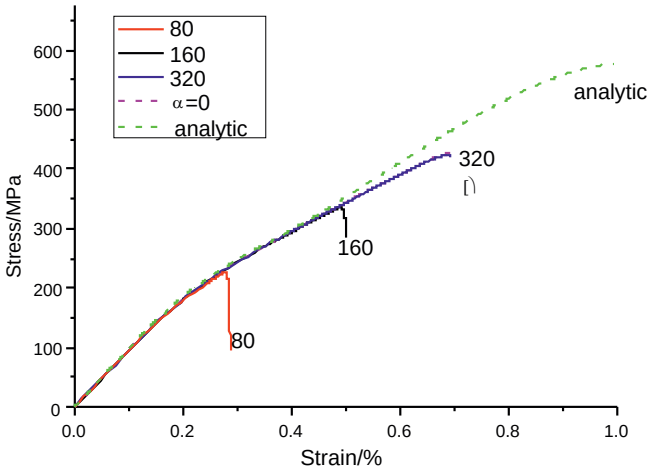

Fig. 11: The stress-strain curves of RVE simulation result with different longitudinal shear strength of tow.

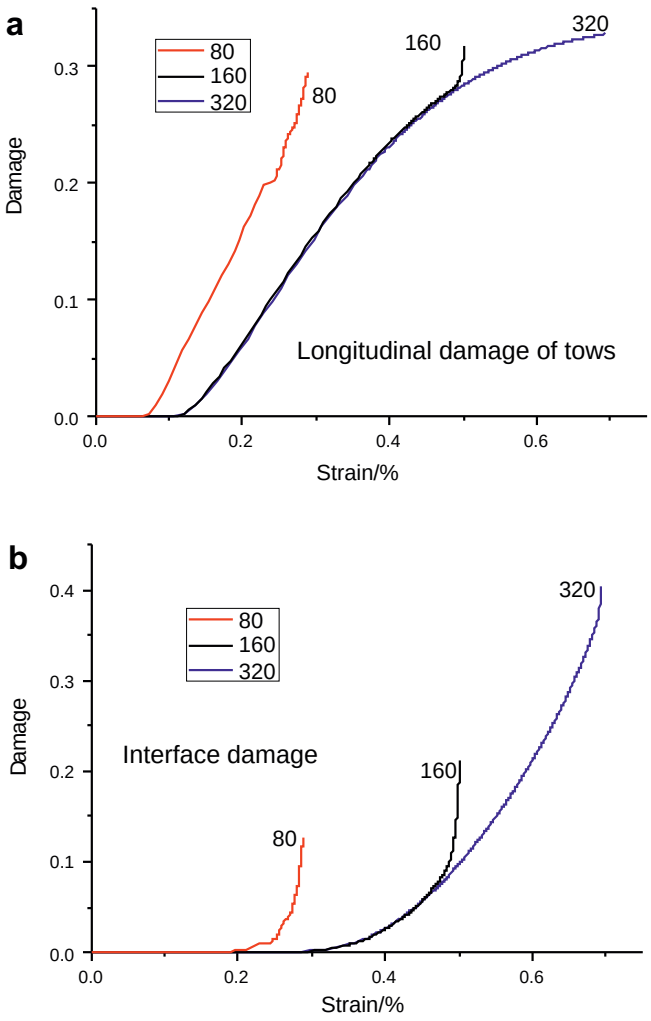

Fig. 12: (a) Longitudinal damage of tows and (b) interface damage evolution curve of RVE simulation results under longitudinal tensile load when shear strength of tow is 80 MPa, 160 MPa, 320 MPa.

Herein, the shear stress threshold was set to a half and double of the value in the previous simulation, and $\alpha = 0$ was also simulated, which means the shear stress did not influence the longitudinal tensile failure of the yarn. The calculated results are shown in Fig. 11. As the shear strength increased from 80 to 320 MPa, the tensile strength was increased from 230 to 425 MPa, respectively, showing a significant influence of shear stress on tensile strength. At $\alpha = 0$, the tensile strength was found to be 425 MPa, which means that the maximum tensile strength was 425 MPa irrespective of the shear stress. However, this value is still lower than the theoretical value and the tensile strength is not only compromised by the shear stress.

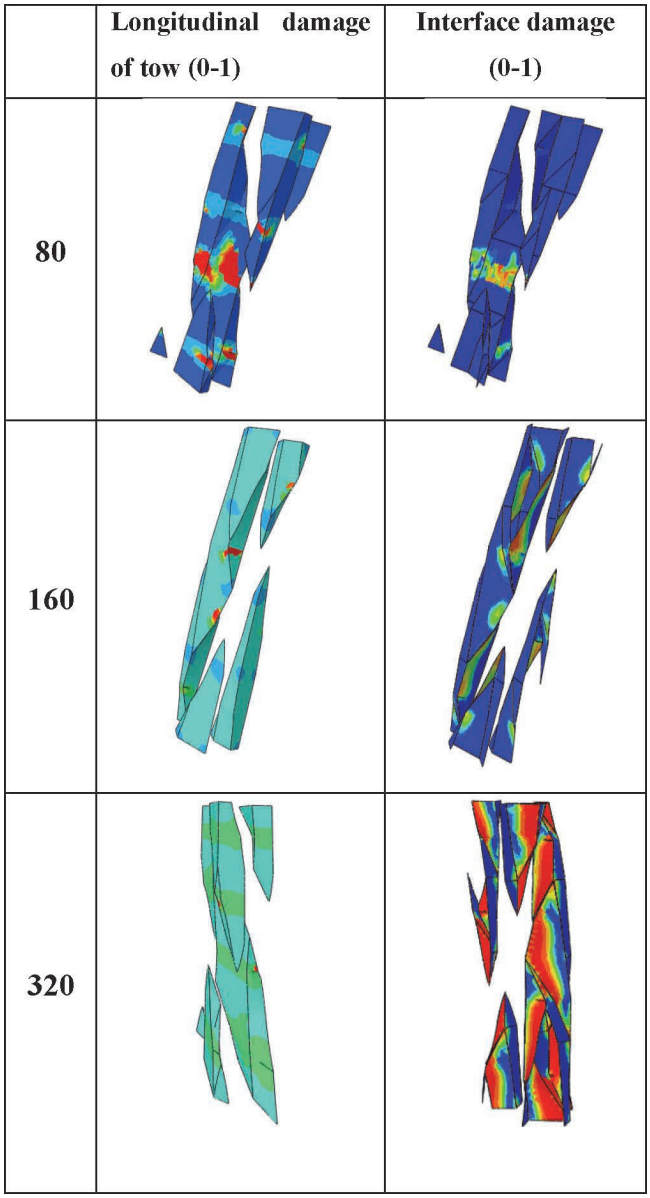

Fig. 13: Meso-scale damage evolution curve, and longitudinal damage of tow and interface damage contour at maximum load of RVE simulation results under longitudinal tensile load when shear strength of tow is (a) 80 MPa, (b) 160 MPa, (c) 320 MPa.

All the simulated stress-strain curves in Fig. 11 are almost the same before the maximum stress points and similar to the theoretical prediction of unidirectional-reinforced CMCs. The damage evolution curve (Fig. 12) and damage distribution (Fig. 13) exhibit that the longitudinal damage of yarns and interface damage are the main damage modes.

Under the low shear strength, the longitudinal damage of yarns evolved faster than the high shear strength. For example, at the shear strength of 80 MPa, when yarns failed at the stress concentration region, the other yarns' elements show a low damage state. When yarns failed at the same region at the shear strength of 160 MPa, the other yarns' element damage state was more severe. Moreover, the interface damage at maximum stress also substantially increases with increasing shear strength (Fig. 12b), which implies that the variation in shear strength influences the interface damage evolution, showing complex damage mode interactions in the RVE.

(b) *Influence of interfacial strength on longitudinal tension*

The yarn/yarn (matrix) interface is mainly a layer of the porous matrix due to the PIP process, which can be adjusted by the process parameters to decrease the porosity and improve the mechanical properties. Herein, the influence of interfacial strength on longitudinal tensile behavior is numerically simulated. Fig. 14 shows the stress-strain curve under longitudinal tensile load when the interfacial strength is 40 MPa, 80 MPa and 160 MPa. The stress-strain curves coincide before the maximum stress and the tensile strength was found to be 280, 335, and 340 MPa, respectively. The results revealed that the effect of interfacial strength was not significant on tensile behavior. Fig. 15a shows the interfacial damage evolution. The interface was almost completely damaged at the interface strength of 40 MPa. However, when the interface strength was 160 MPa, the interface remained undamaged and the ultimate tensile stress did not significantly change. The longitudinal damage evolution of yarns in Fig. 15b also demonstrated that the interface did not influence the yarn damage and, in turn, tensile strength. The simulated results indicate that the interfacial strength may not be the important parameter for the longitudinal tensile properties of the 3D braided composites.

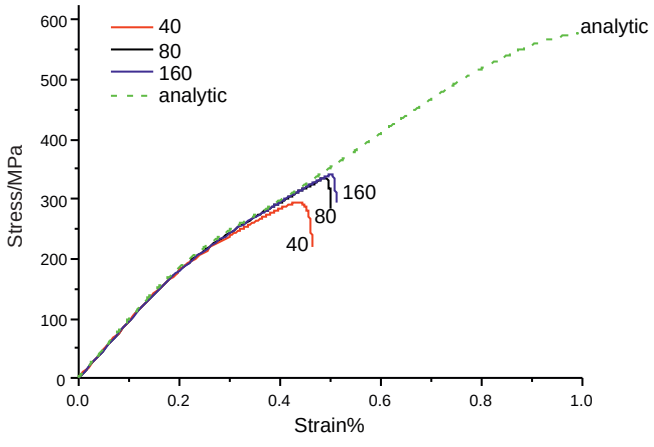

Fig. 14: The stress-strain curves of RVE simulation result with different interface strength of tow.

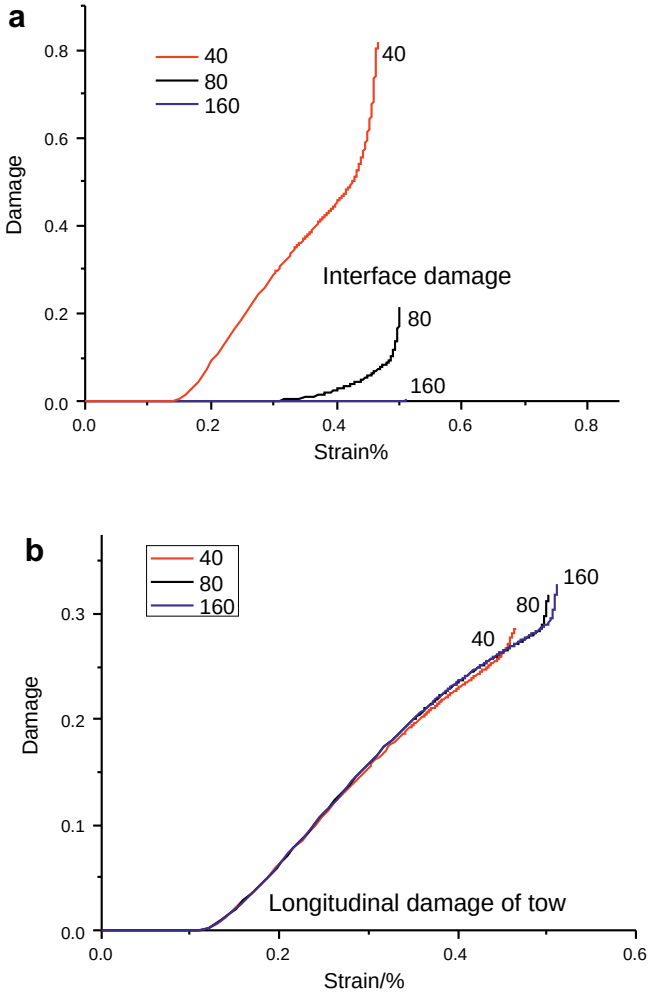

Fig. 15: (a) Interface damage and (b) longitudinal damage of tows evolution curve of RVE simulation results under longitudinal tensile load when interface strength is 40 MPa, 80 MPa, 160 MPa.

(c) *Influence of transverse stress of yarns on transverse tension*

The simulation results demonstrated that the transverse damage of yarns and interface damage were the main failure modes under the transverse tensile load. The influence of the transverse strength of yarns on the transverse tensile strength of composites is investigated based on simulation of the transverse tensile load (S_{22}) of 80 MPa, 160 MPa and 320 MPa (Fig. 16). When the S_{22} was increased to 320 MPa, the strength increased, but the stress-strain curve remained similar to the S_{22} = 160 MPa. However, when the S_{22} was decreased to 80 MPa, a large decrease in strength was observed with a significant change in the stress-strain curve. The stress-strain curve exhibited a plateau after the maximum stress. Fig. 17 shows that the main failure mode is transverse damage of yarns and interface damage at S_{22} = 80 MPa and 320 MPa, respectively. However, a combination of transverse damage of yarns and interface damage was observed at S_{22} = 160 MPa. These results confirm the coexistence and competition between the transverse damage of yarns and interface damage modes under transverse tensile load. When the strength of either the yarns or interface increases the threshold limit, the other one dictates the damage evolution process.

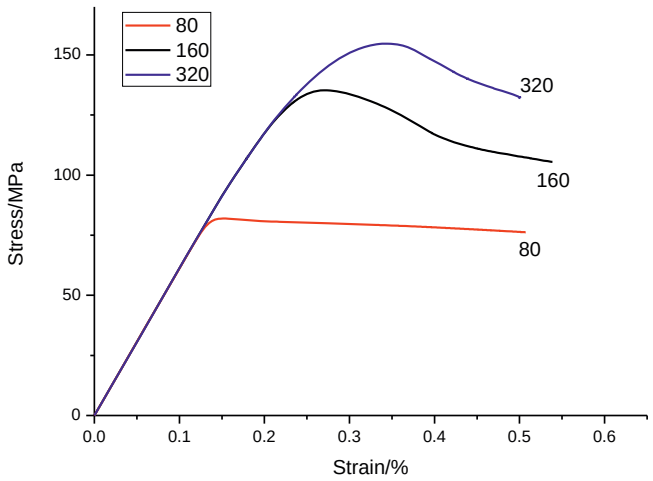

Fig. 16: The stress-strain curves of RVE simulation result under transverse tensile load with different transverse tensile strength of tow.

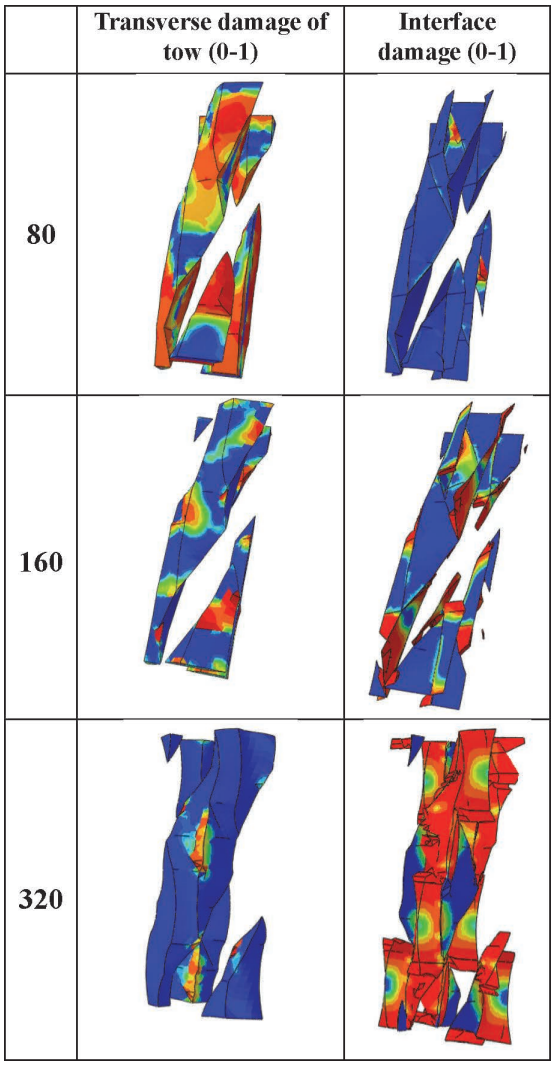

Fig. 17: Meso-scale transverse damage of tow and interface damage contour at maximum load of RVE simulation results under transverse tensile load when transverse tensile strength of tow is (a) 80 MPa, (b) 160 MPa, (c) 320 MPa.

(d) ***Influence of interface strength on transverse tension***

Fig. 18 shows the influence of interface strength (40, 60, 80 and 160 MPa) on transverse tensile strength. The results revealed that the decrease in interface strength lowers the transverse tensile strength. The damage evolution results demonstrated that the interface damage dominates the failure mechanism at the interface strength of 40 MPa (Fig. 19). However, when the interface strength was in-

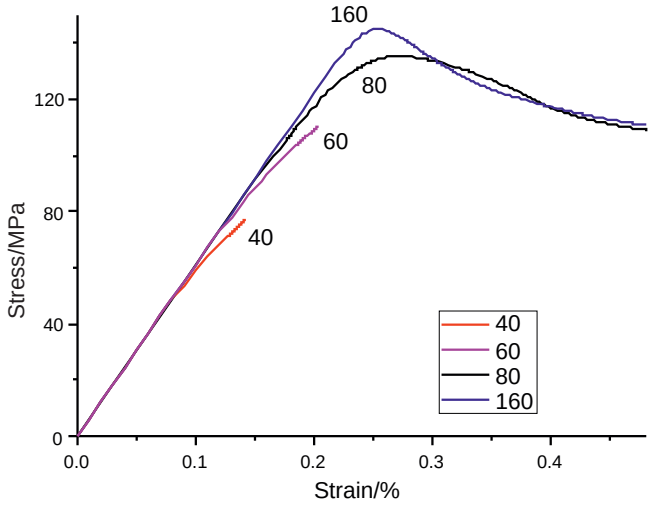

Fig. 18: The stress-strain curves of RVE simulation result under transverse tensile load with different interface strength of tow.

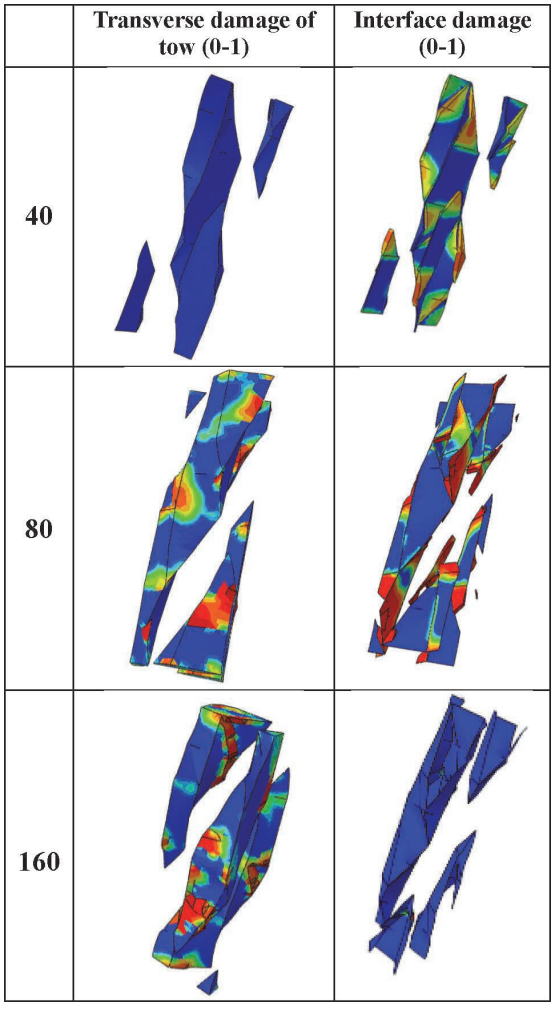

Fig. 19: Meso-scale transverse damage of tow and interface damage contour at maximum load of RVE simulation results under transverse tensile load when interface strength of tow is (a) 40 MPa, (b) 80 MPa, (c) 160 MPa.

creased from 80 MPa to 160 MPa, the increase in transverse tensile strength was not obvious. At the interface strength of 160 MPa, which is equal to the transverse strength of the yarns, the interface remained intact and the transverse damage of the yarns increased compared to the interface strength of 80 MPa. Hence, the key parameter is the change from the interface strength to transverse strength of the yarns. These results confirm the coexistence and competition between the transverse damage of yarns and interface damage under transverse tensile load.

VI. Conclusions

A parametrical study has been conducted to evaluate the influence of meso-scale material properties on macro stress-strain behavior of three-dimensional, four-directional braided SiC/SiC composites. The RVE finite element model, which was built with the aid of μ-CT analysis, was utilized for longitudinal, transverse and off-axis tensile simulations. The off-axis simulation showed that the Tsai-Hill model could be used for multi-axis strength prediction. The longitudinal tensile simulations revealed that the shear strength had a significant impact on longitudinal tensile strength, whereas the influence of the interface damage was not obvious. In addition, the simulation results of the transverse tensile load confirmed that the transverse strength of yarns and interface strength coexisted and competed during the damage evolution process and the inferior one dictated the failure of 3D braided composites under transverse tensile load.

Acknowledgement

This research was supported by the National Natural Science Foundation of China (NSFC 51802264), Natural Science Foundation of Shaanxi Province (2020JQ-177), Fundamental Research Funds for the Central Universities (31020190MS705).

References

1 DiCarlo, J.A., Roode, M.V.: Ceramic composite development for gas turbine engine hot section components. In: ASME Turbo Expo 2006, Power of Land, Sea and Air, 2006.

2 Pluvinage, P., Parvizi-Majidi, A., Chou T.W.: Damage characterization of two-dimensional woven and three-dimensional braided SiC-SiC composites, *J. Mat. Sci*., **31**, [1], 232 – 241, (1996). DOI: 10.1007/BF00355150.

3 Xin, J., Shi, D.Q., Yang, X.G., Zhao, C.J.: Fiber strength measurement for KD-i(f)/sic composites and correlation to tensile mechanical behavior at room and elevated temperatures, *Ceram. Int.*, **41**, [1], 299 – 307, (2015). DOI: 10.1016/j.ceramint.2014.08.072.

4 Lu, S.D., Gao, X.G., Song, Y.D.: Prediction method on equivalent thermal conductivity coefficient of plain braided C/SiC composites material based on finite element method, *J. Aerosp. Power*, **29**, [7], 1574 – 1582, (2014). DOI: 10.13224/j.cnki.jasp.2014.07.009.

5 Shen, X., Liu, X., Dong, S., Gong, L.: RVE model with shape and position defects for predicting mechanical properties of 3D braided CVI-SiCf/SiC composites, *Compos. Struct.*, **195** (JUL.), 325 – 334, (2018). DOI: 10.1016/j.compstruct.2018.04.074

6 Kostar, T.D., Chou, T.W.: Process simulation and fabrication of advanced multi-step three-dimensional braided preforms, *J. Mat. Sci.*, **29**, [8], 2159 – 2167, (1994). DOI: 10.1007/BF01154695.

7 Pandey, R., Hahn, H.T.: Visualization of representative volume elements for three dimensional four step braided composites, *Compos. Sci. Technol.*, **56**, [2], 161 – 170, (1996). DOI: 10.1016/0266 – 3538(95)00137 – 9.

8 Chen, L., Tao, X.M., Choy, C.L.: On the microstructure of three-dimensional braided preforms, *Compos. Sci. Technol.*, **59**, [3], 391 – 404, (1999). DOI: 10.1016/S0266 – 3538(98)00079 – 7.

9 Fang, G.D., Liang J., Yu, W., Wang, B.L.: The effect of yarn distortion on the mechanical properties of 3D four-directional braided composites, *Compos. Part A Appl. Sci. Manuf.*, **40**, [4], 343 – 350, (2009). DOI: 10.1016/j.compositesa.2008.12.007.

10 Li, D.S., Li, J.L., Chen, L., Lu, Z.X., Fang, D.N.: Finite element analysis of mechanical properties of 3D four-directional rectangular braided composites part 1: microgeometry and 3d finite element model, *Appl. Compos. Mater.*, **17**, [4], 373 – 387, (2010). DOI: 10.1007/s10443 – 010 – 9126 – 2.

11 Goldsmith, M.B., Sankar, B.V., Haftka, R.T., Goldberg, R.K.: Quantifying effects of voids in woven ceramic matrix composites. In: 54th AIAA/ASME/ASCE/AHS/ASC Structures, Structural Dynamics, and Materials Conference, Boston, Massachusetts, 2013. DOI: 10.2514/6.2013 – 1619.

12 Naouar, N., Vidal-Sallé, E., Schneider, J., Maire, E., Boisse, P.: Meso-scale FE analyses of textile composite reinforcement deformation based on X-ray computed tomography, *Compos. Struct.*, **116**, [1], 165 – 176, (2014). DOI: 10.1016/j.compstruct.2014.04.026.

13 Straumit, I., Lomov, S.V., Wevers, M.: Quantification of the internal structure and automatic generation of voxel models of textile composites from X-ray computed tomography data, *Compos. Part A Appl. Sci. Manuf.*, **69**, 150 – 158, (2015). DOI: 10.1016/j.compositesa.2014.11.016.

14 Evans, A.G., Zok, F.W.: The physics and mechanics of fibre-reinforced brittle matrix composites, *J. Mat. Sci.*, **29**, [15], 3857 – 3896, (1994). DOI: 10.1007/BF00355946.

15 Lamon, J.: A micromechanics-based approach to the mechanical behavior of brittle-matrix composites, *Compos. Sci. Technol.*, **61**, [15], 2259 – 2272, (2001). DOI: 10.1016/S0266 – 3538(01)00120 – 8.

16 Zhang, D., Hayhurst, D.R.: Prediction of stress-strain and fracture behaviour of an 8-harness satin weave ceramic matrix composite, *Int. J. Solids. Struct.*, **51**, [21 – 22], 3762 – 3775, (2014). DOI: 10.1016/j.ijsolstr.2014.07.010.

17 Fagiano, C., Genet, M., Baranger, E., Ladeveze, P.: Computational geometrical and mechanical modeling of woven ceramic composites at the mesoscale, *Compos. Struct.*, **112**, [1], 146 – 156, (2014). DOI: 10.1016/j.compstruct.2014.01.045.

18 Lu, Z., Wang, C., Xia, B., Yang, Z.: Effect of interfacial properties on the uniaxial tensile behavior of three-dimensional braided composites. *Comp. Mater. Sci.*, 2013, **79**(Complete), 547 – 557, (2013). DOI: 10.1016/j.commatsci.2013.07.017.

19 Fang, G.D., Liang, J., Wang, B.L., Yu, W.: Effect of interface properties on mechanical behavior of 3D four-directional braided composites with large braid angle subjected to uniaxial tension, *Appl. Compos. Mater.*, 18, [5], 449 – 465, (2011). DOI: 10.1007/s10443 – 010 – 9175 – 6.

20 Jing, X., Cheng, Z., Teng, X.F., Yang, X.G., Shi, D.Q.: Reconstruction of meso-structure and numerical simulations of the mechanical behavior of three-dimensional four-directional braided ceramic matrix composites, *Ceram. Int.*, **46**, [18], 29309 – 29320, (2020). DOI: 10.1016/j.ceramint.2020.08.107.

21 Kuhn, J.L., Charalambides, P.G.: Elastic response of porous matrix plain weave fabric composites: Part I-Modeling, *J. Compos. Mater.*, 32(16), 1426 – 1471, (1998). DOI: 10.1177/002199839803201601.

[22] Hashin, Z.: Failure criteria for unidirectional fiber composites, *J. Appl. Mech.*, 47, [2], 329–334, (1980). DOI: 10.1115/1.3157744.

[23] Curtin, W.A.: Theory of mechanical properties of ceramic matrix composites, *J. Am. Ceram. Soc.*, **74**, [11], 2837–2845, (2010). DOI: 10.1111/j.1151–2916.1991.tb06852.x.

[24] Dassault Systemes SIMULIA Corp: Abaqus Analysis User's Manual Version 6.14, (2014).

[25] ASTM D2344/D2344M-16, Standard test method for short-beam strength of polymer matrix composite materials and their laminates, ASTM International, West Conshohocken, PA, 2016.

[26] Rajan, V.P., Zok, F.W.: Matrix cracking of fiber-reinforced ceramic composites in shear, *J. Mech. Phys. Solids*, **73**, 3–21, (2014). DOI: 10.1016/j.jmps.2014.08.007.